COMMUNICATIONS PHYSICS

ARTICLE

Tailoring thermal conduction in anatase TiO$_2$

X. Mettan [1*], J. Jaćimović[1,2*], O.S. Barišić[3*], A. Pisoni[1], I. Batistić[4], E. Horváth[1], S. Brown[1], L. Rossi[1], P. Szirmai [1], B. Farkas[1], H. Berger[5] & L. Forró[1]

Thermal conductivity (κ) plays an essential role in functional devices. It is advantageous to design materials where one can tune κ in a wide range according to its function: single-crystals and nanowires of anatase polymorph of titanium dioxide, broadly used in applications ranging from photovoltaics, reflective coatings to memristors, have been synthesized in large quantities. Here we identify a new, strong diffusion mechanism of heat by polaronic structures due to oxygen vacancies, which considerably influences both the absolute value and the temperature dependence of κ. The additional decrease of κ is achieved in anatase nanowires organized into foam, where porosity and the quasi-one-dimensional size-effect dramatically hinder the propagation of heat, resulting in an extremely low $\kappa = 0.014$ W/Km at room-temperature. Doping this anatase foam could herald promising applications, in particular in thermoelectricity.

[1] Laboratory of Physics of Complex Matter, École Polytechnique Fédérale de Lausanne, 1015 Lausanne, Switzerland. [2] ABB Corporate Research Center, Baden-Daetwill, Switzerland. [3] Institute of Physics, Bijenička c. 46, 10000 Zagreb, Croatia. [4] Department of Physics, Faculty of Science, University of Zagreb, 1000 Zagreb, Croatia. [5] Crystal Growth Facility, École Polytechnique Fédérale de Lausanne, 1015 Lausanne, Switzerland. *email: xmettan@outlook.com; jacim.jacimovic@gmail.com; obarisic@ifs.hr

Active and passive thermal management play a critical role in nearly every sector of engineering sciences. Alongside developing strategies to optimise heat transfer in various devices, understanding and tuning the intrinsic ability of a material to propagate heat is a major issue. Materials with high thermal conductivities (κ) are sought for their capacity to transfer heat swiftly and evenly. Electronic packaging is one of the most important examples where the temperature of a circuit has to be limited to avoid overheating[1–3]. Mediums with high κ are also required in cars, rocket engines, or nuclear reactors, where heat has to be evacuated efficiently to prevent hazardous failure of the mechanical parts. Conversely, other applications demand thermally insulating materials. Compounds with low values of κ ($<0.1\,WK^{-1}m^{-1}$) are employed to prevent severe heat losses in buildings, heat pumps, car engines and power plants[1]. Moreover, thermal conductivity is one of the key parameters ruling the conversion of energy in thermoelectric materials. In the latter case, κ has to be the lowest to enhance the thermoelectric figure of merit[4]. Over the last decade, an ever-intensive scientific effort has been witnessed to develop new technology concepts for producing ultra-low-κ materials. One strategy focuses on structuring a media at meso/nano-scales, thus truncating the phonon-mean-free path[5]. A hundred-fold reduction of the thermal conductivity in silicon nanowires in respect of bulk was reported, and comparable results were obtained in other nanostructured alloys[6]. In a similar approach, compounds with complex cage structures (clathrates, skutterudites) and mixed-lattice atoms (half-Heusler alloys) exhibit low-thermal conductivities[7,8]. Here, the random vibrations of groups of atoms in the lattice hinder the propagation of heat by phonons. Corresponding phenomena have been described in organometallic perovskites, where crystal-liquid duality, together with the formation of large polarons, account for the very low κ[9–11]. Nielsen et al. were reasoning that compounds with anharmonic phonon modes stand amongst the best candidates to moderate heat transport[12]. Although this progress demonstrates the ability to lower κ significantly, fundamental insight into the mechanisms of thermal transport is still needed for designing more efficient materials for thermal management. In addition, many of the proposed low-κ compounds are difficult to scale up for applications, owing to the scarcity of their constitutive elements or to intricate synthesis (e.g. by high-pressure or nano-lithographic processes). Developing materials with few elements and up-scalability is the optimal strategy.

In this context, TiO$_2$ emerges as a prominent candidate, since titanium is the ninth most abundant element on Earth, and TiO$_2$ is non-toxic and stable under atmospheric conditions. It provides a wide spectrum of functionalities for attractive applications, allowed by a variety of different architectures at nanoscales[13]. In particular, photocatalytic activity of thin TiO$_2$ coatings proves antibacterial action and self-cleaning properties[14–16]. These features can also be achieved when titanate nanowires are arranged into a fibrous network, thus providing an enhanced filtering with significant potential for water and air purification[17,18]. Moreover, nanoparticles of TiO$_2$ contribute to good performances of solar-cells regarding the collection of photo-induced charges[19]. For niobium-doped TiO$_2$ a high power-factor was reported, placing this material among promising-thermoelectric converters[20]. Besides energy- and environment-oriented applications, TiO$_2$ nanostructures achieved humidity sensing[21], they were employed to reinforce polystyrene composites[22] and are foreseen as central elements of non-volatile memories (memristors)[23]. Most of the beneficial characteristics of TiO$_2$ stem from the anatase phase of the material. Although thermal conductivity of rutile, another polymorph of TiO$_2$ commonly found in its bulk form, was measured decades ago ($\kappa = 8\,WK^{-1}m^{-1}$ at room-temperature)[24], the same quantity for bulk-anatase crystals or nanowires remains largely unexplored, mainly due to difficulties in synthesis. In the present work their measurements are exposed, and we identify a new, strong diffusion mechanism of heat by polaronic structures due to oxygen vacancies, which considerably influences both the absolute value and the temperature dependence of κ. A further step in decreasing κ is achieved in anatase nanowires organised into foam. In this case, porosity and the quasi-one-dimensional size-effect of thin nanowires dramatically hinder the propagation of heat, resulting in an extremely low $\kappa = 0.014$ W/Km at room-temperature.

Results

Figure 1 shows the broad range of anatase samples for which thermal conductivity is reported here. The large, millimetres-long single-crystals (SC) on Fig. 1a are unique for anatase in which growth our laboratory is specialised. One can easily vary their oxygen stoichiometry, from the pristine one (transparent) on the left, towards the increased concentration of oxygen vacancies (brown and black) achieved by heat treatment in a hydrogen-rich atmosphere. The black SC on the right, from the pristine, 3.2 eV gapped semiconductor, evolved towards a semi-metallic sample due to the shallow-donor levels introduced by the off-stoichiometry[25,26]. Complementarily, electron paramagnetic resonance (EPR) provides a measure of the spin-1/2 defect concentration originated by oxygen vacancies: 0.34, 21 and 51 ppm for the transparent, brown and black crystals respectively (see Supplementary Note 1, Supplementary Figs. 1 and 2). The concentration of defects for another "pristine"-anatase crystal was reported earlier by Chauvet et al., and its value ~15 ppm is an order of magnitude higher than our SC, but far below 10,000 ppm (1%)[27]. In Fig. 1b, the egg-white-like, airy sample (referred to in the following text as "foam") was prepared from the quantity of TiO$_2$ powder exposed in the right Petri-dish, by first transforming it into nanowires. The breakthrough in its preparation is the scaling-up of the growth of nanowires from milligrams (hydrothermal synthesis) to kilograms by a different synthesis route[19]. Figure 1c displays a zoom on the foam by scanning electron microscopy (SEM), revealing the architecture of the nanowires, and Fig. 1d exhibits it after its compression applying 100 MPa of uniaxial pressure. The density and the inter-wire connections are clearly increased. For the sake of completeness, an assembly of anatase nanoparticles (mean diameter 50 nm), already used in many applications, was also prepared and measured (Fig. 1e).

Thermal conductivity of anatase single crystals. Thermal conductivity of anatase SC was measured in the temperature range of 10–300 K; a steady-state, four-point method was applied, described previously by Jaćimović et al.[28]. The three curves in Fig. 2a correspond to the crystals displayed in Fig. 1a, from the top κ of the transparent crystal and below with increasing amounts of oxygen vacancies. A significantly higher value of κ for the more electrically insulating crystals is the first indication that itinerant charge carriers are not the main heat transporters. Indeed, using the Wiedemann-Franz law, even for the most electrically conducting crystal (the black SC), the electronic part κ_{el} is at the level of $10^{-3}\,WK^{-1}m^{-1}$, a negligible fraction of the total κ at room-temperature ($5\,WK^{-1}m^{-1}$)[29]. Consequently, in all our anatase SCs, heat is propagated almost entirely by the phonon subsystem (sketched in Fig. 2b, for the pristine, transparent SC). Using the experimental data in Fig. 2a measured in a broad temperature range, our primary interest is to explain the dramatic drop of κ with increasing concentration of oxygen vacancies. This could greatly help the control of thermal properties of anatase, ranging from SCs to nanostructured materials.
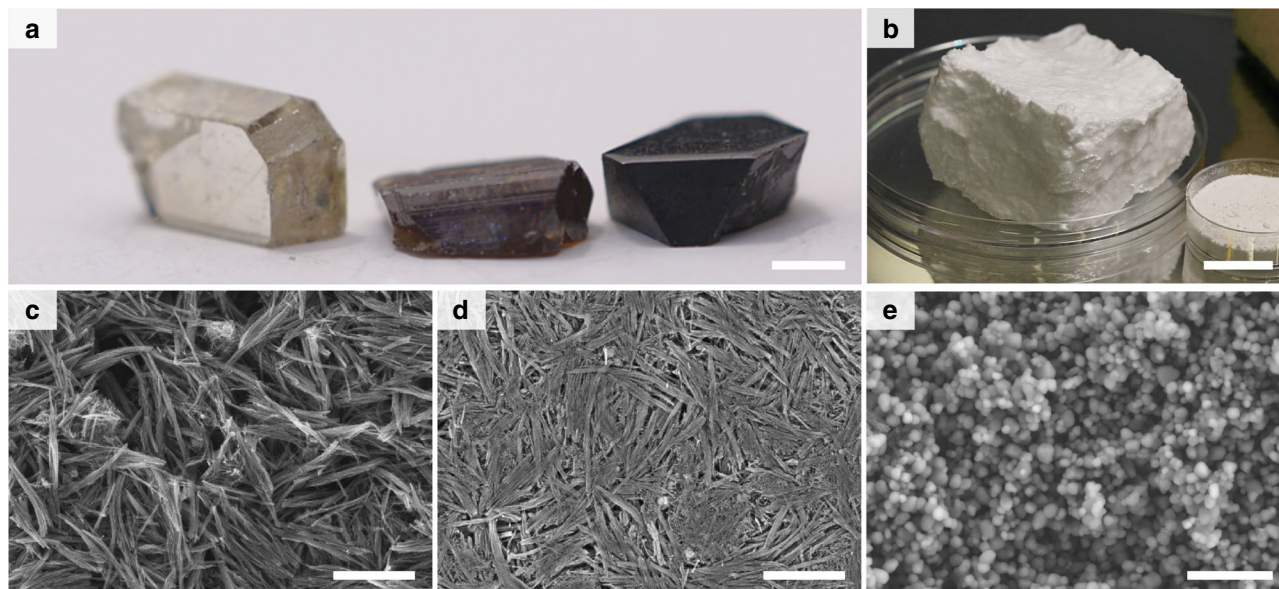
Fig. 1 Anatase single-crystals, foam and nanoparticles. **a** Millimetre-sized single-crystal (SC) of anatase TiO_2. From left to right, insulating (transparent SC) and oxygen richer insulating anatase (brown SC), hydrogen treated conducting anatase (black SC). **b** Photography of the as-grown TiO_2 foam; the jar (bottom right) contains the TiO_2 powder employed for the synthesis of nanowires and nanoparticles. **c–e** Scanning electron microscope micrographs of uncompressed foam, foam compressed (100 MPa) and TiO_2 nanoparticles, respectively. The scale bars correspond to 1 mm in **a**, 20 mm in **b** and 1 µm in **c–e**
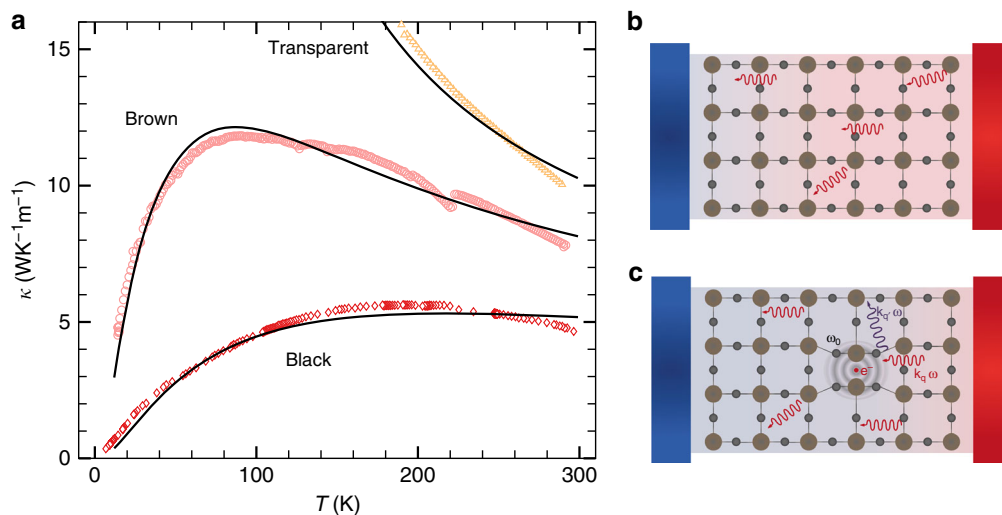

Fig. 2 Thermal conductivity of anatase single-crystals. **a** Temperature dependence of the thermal conductivity of insulating-transparent, brown and conducting-black anatase TiO_2 single-crystals, respectively from higher to lower κ. The solid lines are fits of κ including the resonant-dynamical-scattering term. Sketches of the difference between heat propagation in **b** pristine single-crystal and in **c** crystal with oxygen vacancies. Only one vacancy is displayed with an electron localised in its surrounding. Such defects exhibit strong polaronic effects, which heavily scatter phonons and reduce κ. The colour gradients from red to blue illustrate temperature differences across the material. Experimental error at 300 K is 15%, and decreases with lowering temperature as the black-body-radiation contribution diminishes

Recent ab initio calculations relying on non-perturbative microscopic treatment of static defects characterised by lattice-elastic-constant and mass variances around these defects, demonstrated that standard perturbative approaches can considerably underestimate phonon-scattering rates. Namely, high-order scattering processes may result in large corrections of these rates[30,31], which, if combined with a concentration of defects that surpass 1%, can account for a reduction[32–34] of the thermal conductivity that is comparable to the reduction of $\kappa(T)$ observed in Fig. 2a. However, the concentrations of defects in our SCs (10^{16} cm^{-3}, 6.3×10^{17} and 1.5×10^{18} cm^{-3}, for the transparent,

brown and black SC, respectively) are far below 3×10^{20} cm^{-3} (2–4 orders of magnitude), the threshold corresponding to 1% of defects. This clearly indicates the existence of an additional mechanism for the phonon-scattering that has not been considered so far. In the quest for identifying this extra contribution, we have to recall that Ti–O are dominantly ionic bonds[35,36], which is underlined by a large difference between static (ε_0) and optical (ε_∞) dielectric constants, $\varepsilon_0 >> \varepsilon_\infty$[37]. Therefore, the presence of an excess charge in such medium can significantly affect the surrounding-lattice polarisation (deformation), particularly in the limit of low concentration of

itinerant charge carriers, when the screening is weak, as it is the case in anatase (even for the electrically conducting SC)[38]. Density functional theory (DFT) calculations found a diversity of band-gap states and resonances in anatase TiO_2 (in bulk and at surfaces), for various impurities and intrinsic defects[39,40]. In particular, polaronic defects related to charged-oxygen vacancies in anatase have been reported both theoretically[41,42] and experimentally[26,43]. Atoms in the vicinity of such defects relax to a new equilibrium position due to their strong coupling to the charge in excess, a process that can be compared to the formation of a small-localised polaron[44]. Such a localised-polaronic defect is characterised by a large binding energy $E_b \gtrsim 300$ meV, corresponding to a band-gap state that is, to a great extent, spectrally and spatially decoupled from the rest of the system[45]. A polaronic defect develops its own dynamics, characterised by typical frequencies of its internal excitations $\omega_{p,i}$. Since $E_b >> \hbar\omega_{p,i}$ in the temperature range considered herein (where $k_B T \sim \hbar\omega_{p,i}$), the surplus of electric charge remains well-confined around the vacancy. Moreover, a charged-polaronic defect, involving internal degrees of freedom and their corresponding excitations, interacts with crystalline phonons in its surrounding, contributing importantly to their scattering (sketched in Fig. 2c). This scattering is dynamical, and as such, fundamentally different from static situations described earlier with variances of the lattice parameters. Furthermore, without any screening, the forces are long-ranged, enhancing particularly low-momentum scattering rates. In order to validate this new, polaronic scenario we turn to a standard model giving very reasonable approximations of thermal properties, yet involving a small set of parameters. In this context, we start from the Boltzmann transport equation, using the relaxation time approximation (see Supplementary Notes 2 and 3, Supplementary Eq. (S14))[46]. The total scattering time τ is obtained from Matthiessen's rule, $\tau^{-1} = \sum_i \tau_i^{-1}$, where τ_i represents different frequency- (ω) and temperature- (T) dependent contributions. In the particular situation of semiconducting materials, three sources of scattering are commonly invoked[47,48]: (i) frequency-independent-Casimir scattering rate at the boundaries of the sample $\tau_C^{-1} = a_C = v_s/L$, where v_s is the average speed of sound and L a characteristic dimension of the SC; (ii) frequency-dependent-Rayleigh scattering at static-point-like impurities, $\tau_R^{-1} = a_R\omega^4$; and (iii) anharmonic phonon-phonon (Umklapp) scattering incorporating both ω and T dependencies, $\tau_U^{-1} \sim a_U T\omega^2 exp(-T_U/T)$ (with T_U a characteristic energy for the Umklapp process). Using these three scattering mechanisms only, the best fit of the experimental data for the brown and the black SCs give Casimir-scattering times a_c (Table 1) that are orders of magnitude lower than realistic values. The latter may be estimated from $a_C = v_s/\sqrt{S}$, with the average speed of sound, $v_s \approx 7 \times 10^3$ ms^{-1}, and the characteristic length scale given by the sample cross-section S, similar for all SC samples in Fig. 1,

$\sqrt{S} \approx 10^{-3}$ m. This is a further evidence calling for an additional source of scattering for phonons. As shown in Supplementary Note 2 and 3, the polaronic-scattering mechanism leads to a resonant form of the phonon-relaxation time:

$$\tau_p^{-1}(\omega) = N_d \sum_i b_i \frac{\omega_{p,i}^4}{\left(\omega_{p,i}^2 - \omega^2\right)^2}, \qquad (1)$$

with N_d the concentration of polaronic defects, and b_i constants with dimensions of frequencies, defined by details of their coupling to crystalline phonons. Fitting κ across the whole temperature range with τ_p included, one does not only obtain a qualitative, but also a remarkable quantitative agreement with the experimental data. Striving to retain a minimal number of parameters in our modelling, τ_p in Eq. (1) relies on two resonant frequencies only, yielding $\omega_{p,1} = 7.8$ meV and $\omega_{p,2} = 16.4$ meV.

As discussed in Supplementary Notes 2, these frequencies, characterising internal excitations of polaronic defects, correspond to renormalized-local-phonon modes in the neighbourhood of a vacancy site, adiabatically softened due to the strong polaronic coupling with the charge in excess. Simultaneously, the values of the parameters related to the Casimir-, Rayleigh- and Umklapp- scattering are kept the same for all three SCs, foregrounding the influence of polaronic defects on κ. In other words, the parameter proportional to the concentration of defects N_d is the only one altered, allowing fitting curves to fairly align with the experimental data of the SCs-data in Fig. 2a. From these fits, one finds that N_d in the conducting SC (black) is about one order of magnitude higher than in the insulating SC (brown) (see Supplementary Note 4), in good agreement with the measured concentration of defects[26]. Therefore, we infer that N_d is closely related to the amount of oxygen vacancies in our specimens[26]. To our knowledge, the dynamical phonon-scattering rate $\tau_p^{-1}(\omega)$ was derived for the first time, successfully explaining the reduction of κ in anatase TiO_2 by oxygen vacancies. This mechanism should act in the rutile phase of TiO_2 as well, which has shown a strong dependence on the oxygen stoichiometry[24]. Complementarily to it, a further reduction of κ in anatase was thought to be achievable by texturing the material at micro- and nano- scales. This is precisely the course of action taken and presented hereafter for the anatase nanowires (foams) and nanoparticles displayed in Fig. 1c–e, respectively.

Thermal conductivity of the anatase foams and nanoparticles. The thermal conductivities of the anatase foams and nanoparticles are shown in Fig. 3a, b, mirrored in Fig. 3c–e by sketches of the sample's textures. Compared to the most thermally insulating anatase single-crystal, κ of the as-grown foam is reduced by a factor of 600 at room-temperature, attaining the ultra-low value of $\kappa = 0.014$ WK^{-1}m^{-1}. This number competes with that of

Table 1 Model parameters in Supplementary Eq. (S14) obtained by two fitting procedures (with and without resonant scattering in Callaway's formula), for the thermal conductivity of anatase single-crystals

TiO$_2$	a_C (10^6 s^{-1})	a_R (s^3)	a_U (10^4 K^{-1}s)	θ_D (K)	T_U (K)	a_p (10^8 s^{-1})	ω_1 (K)	ω_2 (K)	α
Black	11,400	616	5.01	1000	600	–	–	–	–
Brown	502	616	5.01	1000	600	–	–	–	–
Black^r	4.56	228	2.29	900	170	39.8	89.7	191	2.76
Brown^r	4.56	228	2.29	900	170	3.63	89.7	191	2.76
Transp.	4.56	228	2.29	900	170	0	–	–	–

a_C, a_R and a_U are the parameters related to Casimir, Rayleigh and Umklapp scattering respectively, with T_U a temperature characteristic of Umklapp processes. Θ_D is the Debye temperature; ω_1 and ω_2 are two resonant frequencies and α an adjustment factor to account for the influence of ω_1 with respect to ω_2. When the resonant scattering is included (superscript r), only a_p, the parameter proportional to the concentration of defects N_d, varies between the single crystals with different amount of oxygen vacancies.
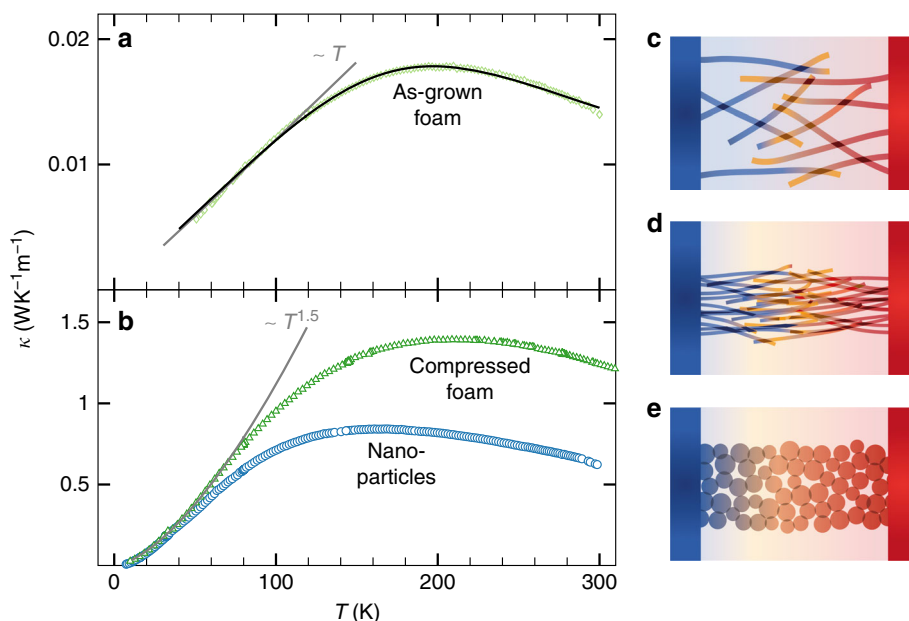
Fig. 3 Thermal conductivity of the anatase foams and nanoparticles. a Temperature dependencies of the thermal conductivity of as-grown and **b** the compressed anatase TiO$_2$ foams (green triangles). The solid lines correspond to fitting curves. The blue circles represent the data for the assembly of nanoparticles. Experimental error at 300 K is 15%, and decreases with lowering temperature as the black-body-radiation contribution diminishes. **c–e** Sketches of the three nanostructures based on their scanning electron micrograph images

organic and silica aerogels at room-temperature and makes anatase foam a (thermal) superinsulator[49]. Yet, structural inhomogeneities and the high porosity of this foam alone ($\varphi = 95\%$) cannot account for such a marked reduction of κ. Indeed, an estimation of the thermal conductivity of the foam κ_f as a sole consequence of the porosity can be obtained within the percolation theory: $\kappa_f = \kappa_b(1-\varphi)^t$, where κ_b is the thermal conductivity of the pristine anatase SC. For $t = 1.5$[50], this estimation gives $\kappa_f = 0.1\,\mathrm{WK^{-1}m^{-1}}$ at room-temperature, an order of magnitude above the experimental value. Hence, reasons for the particularly low value of κ_f and its temperature dependence have to be sought in the peculiar morphology of the foam at nanoscale: properties of individual nanowires composing the foam and the number of contacts between them drastically affect the thermal transport.

On average, anatase nanowires can be approximated as crystalline rods of ~200 nm length and 10 nm diameter[51], with lattice fringes in the [101] plane[19]. As for the contacts between nanowires, transmission-electron microscopy verifies their crystalline nature and their small cross-section (~10 nm), with the [001] crystal orientation across two nanowires[19]. Further analysis of the scanning electron microscopy (SEM) images of the as-grown foam (Figs. 1c and 3c) indicate that each nanowire connects to only few (~3 on average) neighbouring wires, whereas upon compression this number rises to ~25 (Figs. 1d and 3d). Considering a single nanowire, only phonons with momenta aligned along its axis contribute significantly to the heat transport. Namely, the rod's rough boundaries diffusively scatter phonons whose momenta are not aligned along the rod's axis. This effect is enhanced at low temperatures by the small number of unit cells along the rod's diameter, which makes the phonon spectrum strongly gapped for excitations in the perpendicular directions. These effects of reduced dimensionality can be probed at low temperatures, where κ scales as T^β, and β is the effective-low-temperature dimension of the phonon subsystem (see Supplementary Note 5). For the as-grown foam, according to a simple fit, $\beta = 1.0$ (Fig. 3a), which permits the Callaway formula (Supplementary Eq. (S14)) to be implemented with a one-dimensional density of states[52]. Owing to the scarce amount of

defects (2.5 ppm), we deliberately omit the effects of polaronic and static defects. As a result, the fit of the whole temperature dependence of κ in Fig. 3a can hardly be distinguished from the experimental data. At low temperatures, the mean free path l_{ph} (corresponding to phonons with momenta aligned along the rod's axis) is comparable to the average length of nanowires, pointing towards a partially ballistic, quasi-one-dimensional transport between contact areas. However, temperatures higher than one fifth of the Debye temperature ($\Theta_D/5$) prompt Umklapp scattering, hence notably decreasing l_{ph}. We benefit from compaction as a simple and powerful way to continuously tune thermal (and mechanical) properties of the foam. As the porosity drops by ~70%, κ of the compressed foam increases by two orders of magnitude. A larger low-temperature exponent $\beta = 1.5$ (Fig. 3b) supports the drastic change in the nanowires-connectivity scheme after compression. Interestingly, the assembly of TiO$_2$ nanoparticles (Figs. 1e and 3e) exhibit analogous thermal transport properties as the compressed foam (blue dots in Fig. 3b), especially at low temperatures. This suggests that both nanostructured materials are characterised by a similar connectivity scheme in the three-dimensional volume, with a small active portion of nanoparticles surface actually contributing to heat transport (as for nanowires)[53].

Discussion
A summary of our measurements in Fig. 4 shows the outstanding flexibility of anatase TiO$_2$-based materials in tuning thermal conductivity over three orders of magnitudes at 300 K by polaronic and nano-structuring effects. The dynamic-polaronic-scattering mechanism, prompted by charged-oxygen vacancies, has not been discussed before. It has been uncovered by theoretical modelling and found to dominantly account for the reduction of κ in bulk anatase. Yet, beyond oxygen vacancies in anatase, this model encompasses wider classes of defects and impurities, opening the door to a more accurate understanding of polaronic effects on phonon-thermal transport. This also brings attention to the multiple consequences of doping efforts in anatase, many of
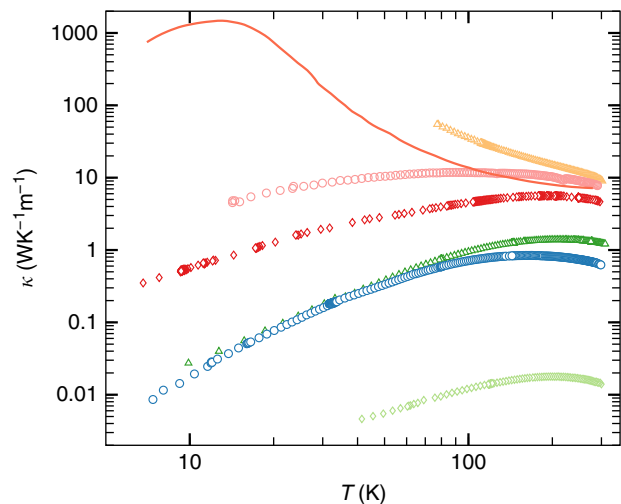
Fig. 4 Overview of the thermal conductivity of single-crystals and textured anatase polymorph of TiO₂. The thermal conductivity of the transparent (orange triangles), brown (pink circles) and conducting-black (red diamonds) single-crystals, compressed (dark green triangles) and as-grown (light green diamonds) foams made of nanowires and of nanoparticles (blue circles), span four orders of magnitude. For comparison, the solid line shows the thermal conductivity of rutile TiO₂ single-crystal, reproduced from the work of Thurber et al.[24]

which aspire to reduce the energy gap and to collect a broader spectral range in photovoltaics. Our study shows that one does not only change the electronic, but substantially the thermal properties as well, through the resonant scattering of phonons on polaronic defects. This fundamentally new finding gains relevance in many other functional oxides, such as $SrTiO_3$, ZnO and $CaMnO_3$, where polarons are present.

Next to that, it is remarkable that in assemblies of nanowires produced in large scales, and not only in lithographically fabricated micron-square surfaces, one can engineer structures with ultra-low-thermal conductivity. The value of $0.014\,WK^{-1}m^{-1}$ is important and beneficial by itself because it calls for an excellent thermal insulator, but especially also by the way it was reached: by the discreet-phonon dispersion due to the one-dimensionality of the nanowires. Since the same mechanism does not limit the electrical conductivity, this foam would be an excellent material for thermoelectric applications if one doped them to metallicity[54]. Recalling that in anatase thin films doped with 6% of Nb, the high power factor ($S^2\sigma$, where S is the Seebeck coefficient and σ the electrical conductivity) of $14\,\mu WK^{-2}cm^{-1}$ gave only a figure of merit (ZT) of 0.1 because of the high thermal conductivity ($8.5\,WK^{-1}m^{-1}$) of the thin film, but not attractive enough for practical purposes. If one could achieve a high σ via doping the nanowires, the foam could deliver a high ZT, and, together with its chemical and high temperatures stability, would be suitable for scalable applications.

Methods
Synthesis of anatase TiO₂ single crystals. Single-crystals of anatase TiO₂ were grown by chemical-vapour transport as described elsewhere[26,29]. Anatase powder of high purity (<300 ppm of Al detected) and powder of NH₄Cl (transport agent) were sealed in a quartz tube in argon gas. The 3-mm-thick, 2-cm-wide, and 20-cm-long ampoule was placed in a horizontal tubular furnace and the temperature at its ends were set to 740 and 610 °C. After 2 weeks, crystals of a few cubic millimetres were grown on the cooler side of the ampoule. The prepared samples are brown, (Fig. 1a), signalling the existence of impurities, while other transparent-stoichiometric samples are colourless with a band gap of 3.2 eV. Earlier, it was demonstrated by Sekiya et al. that this colour indicates the presence of the oxygen vacancies with electrons remaining at their positions[55]. From an energy point of view, these electrons are localised deep in the band gap and do not contribute to the

electrical conductivity. This is confirmed by the measured electrical resistivity of $10^{12}\,\Omega\,cm$ at room-temperature. Several specimens of these crystals were placed in a silica glass tube, inserted into an electric tubular furnace and heated under hydrogen at 650 °C for several hours. Such treatment is known to introduce additional oxygen vacancies whose energetic states are *circa* 100 meV below the conduction band[18,55]. Two effects were observed: the crystals change their colour to dark blue, almost black (Fig. 1b) and electrical resistivity drops to $1\,\Omega\,cm$ at room-temperature. The electrical resistivity measurements showed that such material has metallic character down to 60 K when it starts to behave as insulator, in agreement with earlier findings[25,29].

Synthesis of anatase TiO₂ foams. The preparation of TiO₂ fibrous network (foam) is reported elsewhere[19]. Some of the foam was compressed under a uniaxial pressure of 100 MPa. Pellets were then shaped into parallelepipeds suitable for measurements of κ.

Anatase TiO₂ nanoparticles were bought from Sigma-Aldrich Inc. (powder, −325 mesh, >99% purity) and mixed with polyvinil alcohol (PVA) and poly ethylene glycol (PEG). Secondly the mixture was compressed (380 MPa) to form pellets. In order to completely remove the organic molecules (PVA and PEG), 10 h sintering at 600 °C was performed. As for the foams, evenly shaped samples were obtained by dicing the pellets.

Measurements of thermal conductivity. Thermal conductivity measurements of all specimens were performed using the steady-state method described in the work of Jaćimović et al.[28]. Experimental error at 300 K is 15%, and decreases with lowering temperature as the black-body-radiation contribution diminishes. While, in some cases, anatase is known to host anisotropic physical properties, measurements of κ in different crystallographic directions for the same crystal did not lead to a noticeable anisotropy of this quantity within experimental error.

Measurements of the defect concentrations. Electron paramagnetic resonance (EPR) at 9.4 GHz microwave frequency was performed on a Bruker X-band spectrometer. A conventional field modulation technique was employed with lock-in detection, providing the first derivative of the EPR-absorption spectra. The EPR intensity was calibrated with $CuSO_4 \cdot 5H_2O$ reference samples. The EPR intensity of each signal component is determined both by double integration of the EPR signal and by fitting the (derivative) Lorentzian curves, as is customary in the EPR-related literature[56].

Data availability
The authors declare that all relevant data are included in the paper and its supplementary information files.

References
1. Tong, X. C. *Advanced Materials For Thermal Management Of Electronic Packaging. J. Chem. Inf. Model.* **30**, (Springer, New York, 2011).
2. Papadopoulos, A. M. State of the art in thermal insulation materials and aims for future developments. *Energy Build.* **37**, 77–86 (2005).
3. Balandin, A. A. Thermal properties of graphene and nanostructured carbon materials. *Nat. Mater.* **10**, 569–581 (2011).
4. Snyder, G. J. & Toberer, E. S. Complex thermoelectric materials. *Nat. Mater.* **7**, 105–14 (2008).
5. Hochbaum, A. I. et al. Enhanced thermoelectric performance of rough silicon nanowires. *Nature* **451**, 163–167 (2008).
6. Li, D. et al. Thermal conductivity of individual silicon nanowires. *Appl. Phys. Lett.* **83**, 2934–2936 (2003).
7. Xie, H. et al. Beneficial contribution of alloy disorder to electron and phonon transport in half-heusler thermoelectric materials. *Adv. Funct. Mater.* **23**, 5123–5130 (2013).
8. Nolas, G. S., Poon, J. & Kanatzidis, M. G. Recent developments in bulk thermoelectric materials. *MRS Bull.* **31**, 199–205 (2006).
9. Miyata, K., Atallah, T. L. & Zhu, X.-Y. Lead halide perovskites: crystal-liquid duality, phonon glass electron crystals, and large polaron formation. *Sci. Adv.* **3**, e1701469 (2017).
10. Pisoni, A. et al. Ultra-low thermal conductivity in organic–inorganic hybrid perovskite CH₃NH₃PbI₃. *J. Phys. Chem. Lett.* **5**, 2488–2492 (2014).
11. Lee, W. et al. Ultralow thermal conductivity in all-inorganic halide perovskites. *Proc. Natl Acad. Sci. USA* **114**, 8693–8697 (2017).
12. Nielsen, M. D., Ozolins, V. & Heremans, J. P. Lone pair electrons minimize lattice thermal conductivity. *Energy Environ. Sci.* **6**, 570–578 (2013).
13. Chen, X. & Mao, S. S. Titanium dioxide nanomaterials: synthesis, properties, modifications, and applications. *Chem. Rev.* **107**, 2891–2959 (2007).

14. Heidenau, F. et al. A novel antibacterial titania coating: metal ion toxicity and in vitro surface colonization. *J. Mater. Sci. Mater. Med.* **16**, 883–888 (2005).

15. Szirmai, P. et al. Cyan titania nanowires: spectroscopic study of the origin of the self-doping enhanced photocatalytic activity. *Catal. Today* **284**, 52–58 (2017).

16. Pavlovic, M. et al. Dendrimer-stabilized titanate nanowire dispersions as potential nanocarriers. *J. Phys. Chem. C* **119**, 24919–24926 (2015).

17. Kamegawa, T., Shimizu, Y. & Yamashita, H. Superhydrophobic surfaces with photocatalytic self-cleaning properties by nanocomposite coating of TiO_2 and polytetrafluoroethylene. *Adv. Mater.* **24**, 3697–3700 (2012).

18. Horváth, E., Szilágyi, I., Forró, L. & Magrez, A. Probing titanate nanowire surface acidity through methylene blue adsorption in colloidal suspension and on thin films. *J. Colloid Interface Sci.* **416**, 190–197 (2014).

19. Tétreault, N. et al. High-efficiency solid-state dye-sensitized solar cells: fast charge extraction through self-assembled 3D fibrous network of crystalline TiO_2 nanowires. *ACS Nano* **4**, 7644–7650 (2010).

20. Jaćimović, J. et al. Low temperature resistivity, thermoelectricity, and power factor of Nb doped anatase TiO_2. *Appl. Phys. Lett.* **102**, 013901 (2013).

21. Horváth, E., Ribič, P. R., Hashemi, F., Forró, L. & Magrez, A. Dye metachromasy on titanate nanowires: sensing humidity with reversible molecular dimerization. *J. Mater. Chem.* **22**, 8778 (2012).

22. Byrne, M. T. et al. Chemical functionalisation of titania nanotubes and their utilisation for the fabrication of reinforced polystyrene composites. *J. Mater. Chem.* **17**, 2351 (2007).

23. Yang, J. J. et al. Memristive switching mechanism for metal/oxide/metal nanodevices. *Nat. Nanotechnol.* **3**, 429–433 (2008).

24. Thurber, W. R. & Mante, A. J. H. Thermal conductivity and thermoelectric power of rutile TiO_2. *Phys. Rev.* **139**, A1655–A1665 (1965).

25. Jaćimović, J. et al. High-pressure study of anatase TiO_2. *Materials* **3**, 1509–1514 (2010).

26. Moser, S. et al. Tunable polaronic conduction in anatase TiO_2. *Phys. Rev. Lett.* **110**, 196403 (2013).

27. Chauvet, O., Forro, L., Kos, I. & Miljak, M. Magnetic properties of the anatase phase of TiO_2. *Solid State Commun.* **93**, 667–669 (1995).

28. Jaćimović, J. et al. Enhanced low-temperature thermoelectrical properties of BiTeCl grown by topotactic method. *Scr. Mater.* **76**, 69–72 (2014).

29. Jaćimović, J. et al. Pressure dependence of the large-polaron transport in anatase TiO_2 single crystals. *EPL (Europhys. Lett.)* **99**, 57005 (2012).

30. Polanco, C. A. & Lindsay, L. Thermal conductivity of InN with point defects from first principles. *Phys. Rev. B* **98**, 014306 (2018).

31. Protik, N. H., Carrete, J., Katcho, N. A., Mingo, N. & Broido, D. Ab initio study of the effect of vacancies on the thermal conductivity of boron arsenide. *Phys. Rev. B* **94**, 1–7 (2016).

32. Stern, R., Wang, T., Carrete, J., Mingo, N. & Madsen, G. K. H. Influence of point defects on the thermal conductivity in FeSi. *Phys. Rev. B* **97**, 1–6 (2018).

33. Katre, A., Carrete, J., Dongre, B., Madsen, G. K. H. & Mingo, N. Exceptionally strong phonon scattering by B substitution in cubic SiC. *Phys. Rev. Lett.* **119**, 1–6 (2017).

34. Katcho, N. A., Carrete, J., Li, W. & Mingo, N. Effect of nitrogen and vacancy defects on the thermal conductivity of diamond: an ab initio Green's function approach. *Phys. Rev. B* **90**, 094117 (2014).

35. Asahi, R., Taga, Y., Mannstadt, W. & Freeman, A. J. Electronic and optical properties of anatase TiO_2. *Phys. Rev. B* **61**, 7459–7465 (2000).

36. Landmann, M., Rauls, E. & Schmidt, W. G. The electronic structure and optical response of rutile, anatase and brookite TiO_2. *J. Phys. Condens. Matter* **24**, 195503 (2012).

37. Mahan, G. D. *Many-Particle Physics*. (Springer, US, 2000). https://doi.org/10.1007/978-1-4757-5714-9

38. Gonzalez, R. J., Zallen, R. & Berger, H. Infrared reflectivity and lattice fundamentals in anatase TiO_2. *Phys. Rev. B* **55**, 7014–7017 (1997).

39. Setvin, M. et al. Direct view at excess electrons in TiO_2 rutile and anatase. *Phys. Rev. Lett.* **113**, 086402 (2014).

40. De Angelis, F., Di Valentin, C., Fantacci, S., Vittadini, A. & Selloni, A. Theoretical studies on anatase and less common TiO_2 phases: bulk, surfaces, and nanomaterials. *Chem. Rev.* **114**, 9708–9753 (2014).

41. Mattioli, G., Alippi, P., Filippone, F., Caminiti, R. & Amore Bonapasta, A. Deep versus shallow behavior of intrinsic defects in rutile and anatase TiO_2 polymorphs. *J. Phys. Chem. C* **114**, 21694–21704 (2010).

42. Gerosa, M. et al. Defect calculations in semiconductors through a dielectric-dependent hybrid DFT functional: the case of oxygen vacancies in metal oxides. *J. Chem. Phys.* **143**, 134702 (2015).

43. Moser, S. et al. Electron-phonon coupling in the bulk of anatase TiO_2 measured by resonant inelastic X-Ray spectroscopy. *Phys. Rev. Lett.* **115**, 096404 (2015).

44. Barišić, O. S. & Barišić, S. Phase diagram of the Holstein polaron in one dimension. *Eur. Phys. J. B* **64**, 1–18 (2008).

45. Ko, K. C., Lamiel-García, O., Lee, J. Y. & Illas, F. Performance of a modified hybrid functional in the simultaneous description of stoichiometric and reduced TiO_2 polymorphs. *Phys. Chem. Chem. Phys.* **18**, 12357 (2016).

46. Callaway, J. Model for lattice thermal conductivity at low temperatures. *Phys. Rev.* **113**, 1046–1051 (1959).

47. Casimir, H. B. G. Note on the conduction of heat in crystals. *Physica* **5**, 495–500 (1938).

48. Carruthers, P. Theory of thermal conductivity of solids at low temperatures. *Rev. Mod. Phys.* **33**, 92–138 (1961).

49. Lu, X. et al. Thermal conductivity of monolithic organic aerogels. *Science* **255**, 971–2 (1992).

50. Kirkpatrick, S. Percolation and conduction. *Rev. Mod. Phys.* **45**, 574–588 (1973).

51. Allen, P. B. Nanocrystalline nanowires: 2. Phonons. *Nano Lett.* **7**, 11–14 (2007).

52. Cahill, D. G. et al. Nanoscale thermal transport. II. 2003-2012. *Appl. Phys. Rev.* **1**, 1–45 (2014).

53. Prasher, R. S. et al. Turning carbon nanotubes from exceptional heat conductors into insulators. *Phys. Rev. Lett.* **102**, 1–4 (2009).

54. Jaćimović, J. et al. From nanotubes to single crystals: Co doped TiO_2. *APL Mater.* **1**, 032111 (2013).

55. Sekiya, T. et al. Defects in anatase TiO_2 single crystal controlled by heat treatments. *J. Phys. Soc. Jpn.* **73**, 703–710 (2004).

56. Szirmai, P. et al. Density of states deduced from ESR measurements on low-dimensional nanostructures; benchmarks to identify the ESR signals of graphene and SWCNTs. *Phys. Status Solidi Basic Res.* **248**, 2688–2691 (2011).

Acknowledgements

Author contributions

H.B., E.H. and S.B. synthesized the samples. J.J., A.P. and X.M. performed the measurements of thermal conductivities. L.R., S.B. and X.M. acquired SEM images. P.Sz. and B.F. acquired and analysed the EPR spectra. I.B. and O.S.B. analysed the data, and developed the theoretical description of κ. The project was initiated and coordinated by L.F. The manuscript was written by J.J., X.M., O.S.B. and L.F.

Competing interests

The authors declare no competing interests.

Additional information

Supplementary information accompanies this paper at https://doi.org/10.1038/s42005-019-0224-7.

Correspondence and requests for materials should be addressed to X.M., J.J or O.S.B.

Reprints and permission information is available at http://www.nature.com/reprints

Publisher's note Springer Nature remains neutral with regard to jurisdictional claims in published maps and institutional affiliations.